

A methodology to compute GPS slant total delays in a numerical weather model

Florian Zus,¹ Michael Bender,¹ Zhiguo Deng,¹ Galina Dick,¹ Stefan Heise,¹ Ming Shang-Guan,¹ and Jens Wickert¹

Received 29 August 2011; revised 2 March 2012; accepted 8 March 2012; published 24 April 2012.

[1] A numerical algorithm based on Fermat's Principle was developed to simulate the propagation of Global Positioning System (GPS) radio signals in the refractivity field of a numerical weather model. The unique in the proposed algorithm is that the ray-trajectory automatically involves the location of the ground-based receiver and the satellite, i.e. the posed two-point boundary value problem is solved by an implicit finite difference scheme. This feature of the algorithm allows the fast and accurate computation of the signal travel-time delay, referred to as Slant Total Delay (STD), between a satellite and a ground-based receiver. We provide a technical description of the algorithm and estimate the uncertainty of STDs due to simplifying assumptions in the algorithm and due to the uncertainty of the refractivity field. In a first application, we compare STDs retrieved from GPS phase-observations at the German Research Centre for Geosciences Potsdam (GFZ STDs) with STDs derived from the European Center for Medium-Range Weather Forecasts analyses (ECMWF STDs). The statistical comparison for one month (August 2007) for a large and continuously operating network of ground-based receivers in Germany indicates good agreement between GFZ STDs and ECMWF STDs; the standard deviation is 0.5% and the mean deviation is 0.1%.

Citation: Zus, F., M. Bender, Z. Deng, G. Dick, S. Heise, M. Shang-Guan, and J. Wickert (2012), A methodology to compute GPS slant total delays in a numerical weather model, *Radio Sci.*, 47, RS2018, doi:10.1029/2011RS004853.

1. Introduction

[2] Radio signals transmitted by GPS (Global Positioning System) satellites, traverse the atmosphere before they are recorded by ground-based receivers. Refraction in the atmosphere changes the phase and amplitude of the signals. From GPS dual-frequency phase-observations the signal travel-time delay induced by the neutral atmosphere, in this study referred to as the STD (Slant Total Delay), can be retrieved. Conversely, provided that the refractivity field is known, e.g. given by a NWM (Numerical Weather Model) analysis, STDs can be computed. A method to compute STDs for a given refractivity field is required in both, meteorological and geodetic applications. Potential applications in GPS meteorology [Bevis *et al.*, 1992] include variational data assimilation and least-travel time tomography [Järvinen *et al.*, 2007; Bender *et al.*, 2010]. A typical application in geodesy is the determination of mapping functions [Rocken *et al.*, 2001; Boehm *et al.*, 2006].

[3] The computation of the propagation of radio signals in a refractivity field is based on Fermat's principle: the path taken by a ray between the satellite and the ground-based receiver is the path that can be traversed in the least time. From calculus of variations the ray-trajectory equation is derived and solved by a numerical algorithm. To date a number of different algorithms exist [Mendes, 1999; Pany, 2002; Nievinski, 2009]. Fast and accurate algorithms were recently summarized and analyzed by Hobiger *et al.* [2008]. In essence, all of them have in common that the ray-trajectory equation is solved as an initial value problem. In this study we present an alternative algorithm; the ray-trajectory equation is solved directly as a boundary value problem. The algorithm yields a similar performance, regarding the accuracy and the computational speed. In addition, we estimate the uncertainty of STDs due to simplifying assumptions in the algorithm and we estimate the uncertainty of STDs due to the uncertainty of the refractivity field. The algorithm is particularly suited to compute STDs for a large and continuously operating network of ground-based receivers. In a first application, we compare STDs retrieved from GPS phase-observations with STDs derived from the ECMWF (European Center for Medium-Range Weather Forecasts) analysis.

[4] This paper is structured as follows. In section 2 we provide a technical description of the algorithm. In section 3 we study the accuracy and the computational speed of the

¹GPS/GALILEO Earth Observation, Helmholtz Centre Potsdam, German Research Centre for Geosciences, Potsdam, Germany.

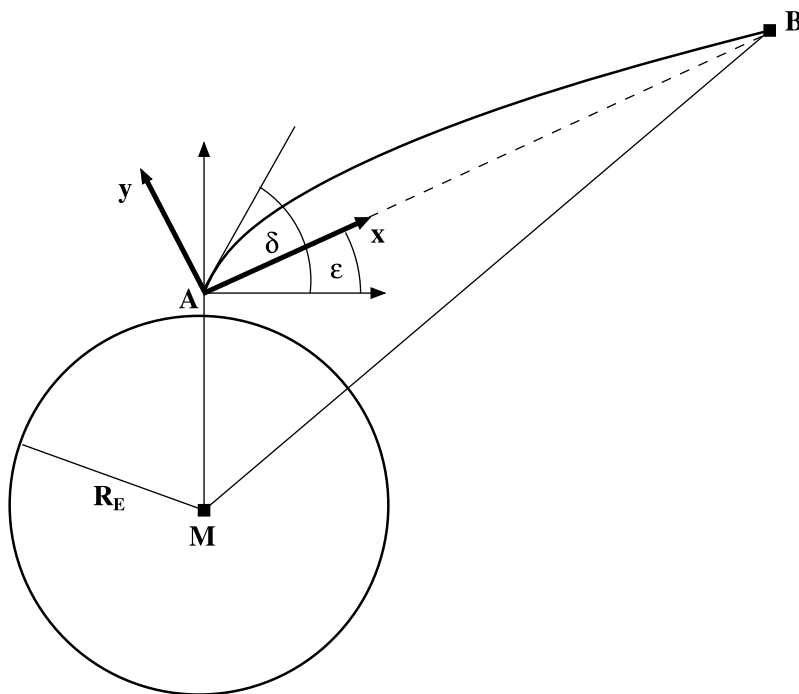


Figure 1. Sketch of the geometry for computing STDs. The location of the receiver is marked with A , the location of the satellite is marked with B and Earth's center is marked with M . R_E denotes the radius of Earth. ε denotes the geometric angle at the receiver and δ denotes the arriving elevation angle at the receiver. The signal path from the satellite to the receiver is indicated by the curved solid line.

algorithm. In section 4 the algorithm is used to compare STDs retrieved from the GPS phase-observations with STDs derived from meteorological analyses. Section 5 summarizes the main results.

2. Technical Description

2.1. The Geometry

[5] Figure 1 provides a sketch of the geometry for computing STDs. The radio signal transmitted by the satellite B traverses the atmosphere before it is recorded by the ground based receiver A . The signal path, indicated by the curved solid line, obeys the ray-trajectory equation (to be described hereinafter). Due to the bending effect of the atmosphere on the signal path, the arriving elevation (azimuth) angle of the signal at the receiver is different from the vacuum elevation (azimuth) angle at the receiver. The geometric path corresponds to the straight dotted line connecting the receiver and the satellite. Hereinafter, the orthonormal system located at Earth's center will be referred as the global frame of reference. The orthonormal system located at the receiver will be referred as the local frame of reference. Note that the receiver is not necessarily located on the Earth surface. The Earth is assumed to be a perfect sphere with radius R_E equal to Earth's mean radius of curvature at the center point of the limited area NWM domain, i.e. $R_E = \sqrt{MN}$, where M and N are the radii of curvature of the meridian and the prime vertical respectively. On the uncertainty of STDs due to this assumption the reader is referred to section 3.

2.2. The Slant Total Delay

[6] The STD, the optical path length minus the geometric path length, is defined as [Hofmann-Wellenhof et al., 1992]

$$S = \int_s n ds - \int dg. \quad (1)$$

[7] Here n denotes the index of refraction, s denotes the signal path and g denotes the geometric path. The ray-trajectory $(x, y(x), z(x))$ is determined through Fermat's principle: The path taken by a ray between the position of the satellite (b, y_b, z_b) and the position of the receiver (a, y_a, z_a) is the path that can be traversed in the least time. From the fundamental lemma of calculus of variation it follows that the ray-trajectory minimizes the optical path length

$$P = \int_a^b n(x, y(x), z(x)) \sqrt{1 + y'(x)^2 + z'(x)^2} dx \quad (2)$$

if and only if the integrand $f = n(x, y, z) \sqrt{1 + y'^2 + z'^2}$ verifies the Euler-Lagrange equation

$$\begin{aligned} \frac{d}{dx} \frac{\partial f}{\partial y'} - \frac{\partial f}{\partial y} &= 0 \\ \frac{d}{dx} \frac{\partial f}{\partial z'} - \frac{\partial f}{\partial z} &= 0 \end{aligned} \quad (3)$$

[8] After some algebra, the following system of equations is deduced

$$\begin{aligned} y'' &= \left(\frac{n_y}{n} - \frac{n_x}{n} y' \right) (1 + y'^2 + z'^2) \\ z'' &= \left(\frac{n_z}{n} - \frac{n_x}{n} z' \right) (1 + y'^2 + z'^2) \end{aligned} \quad (4)$$

[9] Here the subscripts x , y and z denote partial derivatives. With explicit boundary conditions according to

$$\begin{aligned} y(a) &= y_a \\ z(a) &= z_a \\ y(b) &= y_b \\ z(b) &= z_b \end{aligned} \quad (5)$$

the ray-trajectory equation represents a non-linear two-point BVP (Boundary Value Problem). Provided that the index of refraction is known, the ray-trajectory and subsequently the STD can be computed.

2.3. The Index of Refraction

[10] The index of refraction n is related to the refractivity N through

$$n = 10^{-6}N + 1. \quad (6)$$

[11] The refractivity N is related to the partial pressure of dry air p_d , the partial pressure of water vapor p_w and the temperature T through [Thayer, 1974]

$$N = k_1 \frac{p_d}{T} + k_2 \frac{p_w}{T} + k_3 \frac{p_w}{T^2}. \quad (7)$$

[12] The empirically determined constants k_1 , k_2 and k_3 are given by Bevis *et al.* [1994] In a NWM the pressure p , the temperature T and the specific humidity q are typically stored at grid points specified by longitude, latitude and geopotential height. The partial pressure of water vapor is obtained from

$$p_w = \frac{qp}{\epsilon + (1 - \epsilon)q} \quad (8)$$

where $\epsilon = R_d/R_w$. Here R_d and R_w denote the specific gas constant for dry and wet air respectively. The partial pressure of dry air is obtained from $p_d = p - p_w$. The geopotential height is converted to the geometric height above the geoid following M. J. Mahoney (A discussion of various measures of altitudes, 2001, available at <http://mtp.mjmahoney.net/www/notes/altitude/altitude.html>). To compute the refractivity at an arbitrary point a coordinate transformation routine and an interpolation routine is needed. For details the reader is referred to Appendix A.

2.4. The Finite Difference Scheme

[13] The ray-trajectory equation is form invariant. It is convenient to rotate the local frame of reference such that the x -axis points from the receiver to the satellite in question. The ray-trajectory equation is solved in this local frame of reference.

[14] Let x_i for $i = 0, \dots, m + 1$ denote a non-uniform sequence of nodes for which the solution y_i and z_i for

$i = 0, \dots, m + 1$ is sought. The derivatives of y and z with respect to x are approximated by

$$\begin{aligned} y'(x_j) &= \sum_{k=j-1}^{j+1} \ell'_{j,k}(x_j) \cdot y_k \\ z'(x_j) &= \sum_{k=j-1}^{j+1} \ell'_{j,k}(x_j) \cdot z_k \\ y''(x_j) &= \sum_{k=j-1}^{j+1} \ell''_{j,k}(x_j) \cdot y_k \\ z''(x_j) &= \sum_{k=j-1}^{j+1} \ell''_{j,k}(x_j) \cdot z_k \end{aligned} \quad (9)$$

for $j = 1, \dots, m$. Here

$$\ell_{j,k}(x) = \prod_{p=j-1, p \neq k}^{j+1} \frac{(x - x_p)}{(x_k - x_p)} \quad (10)$$

for $j = 1, \dots, m$ denote Lagrange basis polynomials. Inserting the $2m$ finite differences into the ray-trajectory equation leads to a system of $2m$ non-linear algebraic equations for $2m$ unknowns

$$\begin{aligned} \sum_{k=j-1}^{j+1} \ell''_{j,k}(x_j) y_k - \left[\frac{n_y(x_j, y_j, z_j)}{n(x_j, y_j, z_j)} - \frac{n_x(x_j, y_j, z_j)}{n(x_j, y_j, z_j)} \left(\sum_{k=j-1}^{j+1} \ell'_{j,k}(x_j) y_k \right) \right] \\ \cdot \left[1 + \left(\sum_{k=j-1}^{j+1} \ell'_{j,k}(x_j) y_k \right)^2 + \left(\sum_{k=j-1}^{j+1} \ell'_{j,k}(x_j) z_k \right)^2 \right] = 0 \\ \sum_{k=j-1}^{j+1} \ell''_{j,k}(x_j) z_k - \left[\frac{n_z(x_j, y_j, z_j)}{n(x_j, y_j, z_j)} - \frac{n_x(x_j, y_j, z_j)}{n(x_j, y_j, z_j)} \left(\sum_{k=j-1}^{j+1} \ell'_{j,k}(x_j) z_k \right) \right] \\ \cdot \left[1 + \left(\sum_{k=j-1}^{j+1} \ell'_{j,k}(x_j) y_k \right)^2 + \left(\sum_{k=j-1}^{j+1} \ell'_{j,k}(x_j) z_k \right)^2 \right] = 0 \end{aligned} \quad (11)$$

for $j = 1, \dots, m$ with

$$\begin{aligned} y_0 &= 0 \\ z_0 &= 0 \\ y_{m+1} &= 0 \\ z_{m+1} &= 0 \end{aligned} \quad (12)$$

[15] In short term notation the system of equations reads as

$$F(Z) = 0 \quad (13)$$

where $Z = [y_1, z_1, \dots, y_m, z_m]$ denotes the solution vector.

[16] Newton's method is applied to solve the non-linear system of equations. Let Z_r denote the solution vector at the iteration step r . The solution vector Z_{r+1} at the iteration step $r + 1$ is obtained by solving the following system of linear equations

$$\mathbf{J}[Z_r](Z_{r+1} - Z_r) = -F(Z_r) \quad (14)$$

where \mathbf{J} denotes the Jacobian

$$\mathbf{J} = \frac{\partial F}{\partial Z}. \quad (15)$$

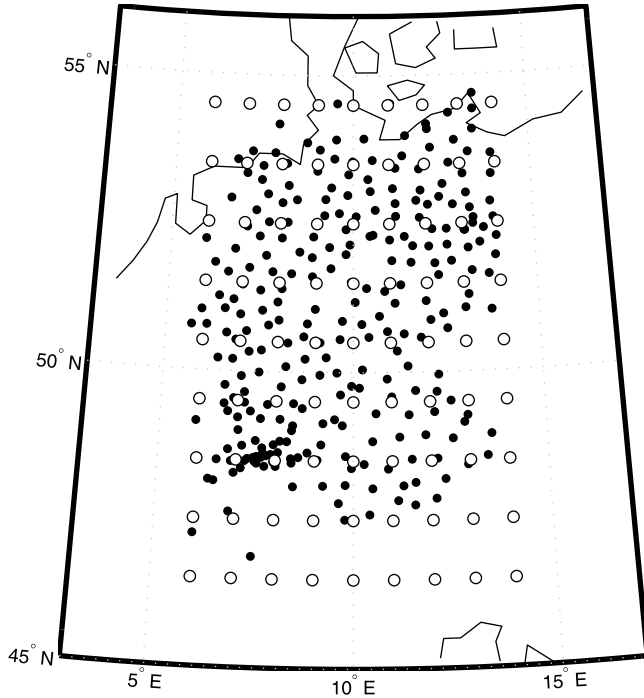


Figure 2. The NWG domain and the location of hypothetical (indicated by white dots) and existing (indicated by black dots) ground-based receivers.

[17] The non-zero entries of the Jacobian are derived by rigorous application of the chain rule of differential calculus. The linear system of equation is solved by LU-Decomposition. The first guess vector is chosen to be equal to the coordinates of points along the geometric path connecting the first and the last node, i.e. $Z = [0, 0, \dots, 0, 0]$.

[18] Once the ray-trajectory is determined, the STD is computed according to

$$S = \sum_{i=0}^{m+1} n(x_i, y_i, z_i) \sqrt{1 + y'(x_i)^2 + z'(x_i)^2} w_i - \sum_{i=0}^{m+1} w_i. \quad (16)$$

[19] Here w_i for $i = 0, \dots, m + 1$ denote quadrature weights according to the trapezoidal rule. The derivative at the first (last) node is approximated by a forward (backward) finite difference. The iteration is stopped if the difference between the current STD and the previous STD is smaller than a user-defined threshold (by default 1 mm). Alternatively, the iteration can be stopped after a predefined number of iterations are performed. For details the reader is referred to section 3.

2.5. Approximations

[20] Two approximations enhance the computational efficiency without altering the accuracy significantly. Both approximations are based on the fact that the refractive index n is more or less stratified with respect to height h . At first, the algorithm is restricted to a plane defined by the center of the Earth, the receiver and the satellite (the x-z plane). Second, the partial derivative of the refractivity with respect

to longitude and latitude at any point is neglected. Thus, we consider the following system of m non-linear algebraic equations for m unknowns

$$\sum_{k=j-1}^{j+1} \ell'_{j,k}(x_j) z_k - \frac{n_h(x_j, z_j)}{n(x_j, z_j)} \left[h_z(x_j, z_j) - h_x(x_j, z_j) \left(\sum_{k=j-1}^{j+1} \ell'_{j,k}(x_j) z_k \right) \right] \cdot \left[1 + \left(\sum_{k=j-1}^{j+1} \ell'_{j,k}(x_j) z_k \right)^2 \right] = 0 \quad (17)$$

for $j = 1, \dots, m$ with

$$\begin{aligned} z_0 &= 0 \\ z_{m+1} &= 0 \end{aligned} \quad (18)$$

[21] The non-linear system of equations is solved by Newton's method. The STD is computed according to

$$S = \sum_{i=0}^{m+1} n(x_i, z_i) \sqrt{1 + z'(x_i)^2} w_i - \sum_{i=0}^{m+1} w_i. \quad (19)$$

[22] It is important to note that the approximations do not imply that the refractivity is a function of the height only. The errors introduced by the approximations are analyzed in section 3.

2.6. The Node-Sequence

[23] The sequence of nodes x_i for $i = 0, \dots, m + 1$ for which the solution y_i and z_i for $i = 0, \dots, m + 1$ is sought was yet not specified. In fact, the sequence of nodes can be chosen arbitrary (except for the first and the last node) and a successive refinement of nodes can be performed to compute the STD with a predefined error tolerance. For example, we may define a uniform sequence of nodes, compute the ray-trajectory and estimate the STD. Then the number of nodes is doubled, the computation of the ray-trajectory is repeated, and another estimate of the STD is obtained. This procedure is repeated until the difference of the current STD and the previous STD is smaller than some predefined error tolerance. For better computational efficiency, it is convenient to use a non-uniform sequence of nodes. We propose the following ansatz:

$$x_i = r_a \cos(\theta) + \sqrt{d_i^2 - r_a^2 \sin^2(\theta)} \quad (20)$$

for $i = 0, \dots, m + 1$ with

$$\begin{aligned} d_0 &= r_a \\ d_i &= r_a + (r_t - r_a) \frac{\exp(\lambda)^i - 1}{\exp(\lambda)^m - 1} \quad i = 1, \dots, m \\ d_{m+1} &= r_b \end{aligned} \quad (21)$$

and

$$\begin{aligned} r_a &= R_E + h_a \\ r_t &= R_E + h_t \\ r_b &= R_E + h_b \\ \theta &= \varepsilon + \frac{\pi}{2} \end{aligned} \quad (22)$$

[24] Here h_a denotes the height of the receiver, h_t denotes the height of the hypothetical top of the atmosphere, h_b

Table 1. Summary of Different Configurations in the STD Algorithm^a

Solution	Approximation	Node-Sequence	Earth	Interpolation
A	no	A	sphere	bilinear
B	no	B	sphere	bilinear
C	no	C	sphere	bilinear
R	no	R	sphere	bilinear
A'	yes	A	sphere	bilinear
B'	yes	B	sphere	bilinear
C'	yes	C	sphere	bilinear
D'	yes	A	ellipsoid	bilinear
E'	yes	A	sphere	bicubic

^aThe configurations differ by the approximations, the node-sequence, the interpolation routine and the shape of the Earth (for details refer to the text).

denotes the height of the satellite, ε denotes the elevation angle and λ denotes the lapse rate of the node-sequence. Essentially, this node-sequence takes into account that the refractivity tends to decrease exponentially with height. By default, we set $m = 800$, $h_t = 150$ km, and $\lambda = 10^{-2}$. In the following this sequence of nodes is referred to as the default node-sequence.

3. Algorithm Performance

[25] In a numerical experiment the accuracy and the computational speed of the algorithm are estimated. For this purpose, refractivity fields are derived from ECMWF

analyses. Analyses are available at 0, 6, 12 and 18 UTC for the DOY (Day Of Year) 230–236 in the year 2007. The idea behind a number of different analysis is to cover the variability of ECMWF refractivity fields. Figure 2 shows the location of hypothetical receivers located at some model terrain grid points. Hypothetical satellites are located at an altitude of 20200 km. We use the default node-sequence and compute STDs at each receiver for elevation angles 1° – 90° (stepsize 1°) and azimuthal angles 45° – 315° (stepsize 90°). By default, we use three iterations in Newton's method. STDs exhibit a strong elevation angle dependency. Roughly speaking, the elevation angle dependency of STDs follows a cosecant law. For an elevation angle of 90° (in the zenith) STDs are ~ 2.4 m, for an elevation angle of 5° STDs are ~ 24 m.

3.1. Accuracy

[26] The node-sequence is successively refined by node insertion; in the following referred to as the node-sequence A (the default node-sequence), B, C and R. For the node-sequence A, B, C and R we compute STDs (we use three iterations in Newton's method); in the following referred to as solution A, B, C and R. The solution R serves as the reference solution. The main characteristics of the solutions are summarized in Table 1. The accuracy is measured in terms of the root-mean square deviation from the reference solution. Figure 3 shows the root-mean square deviation as a

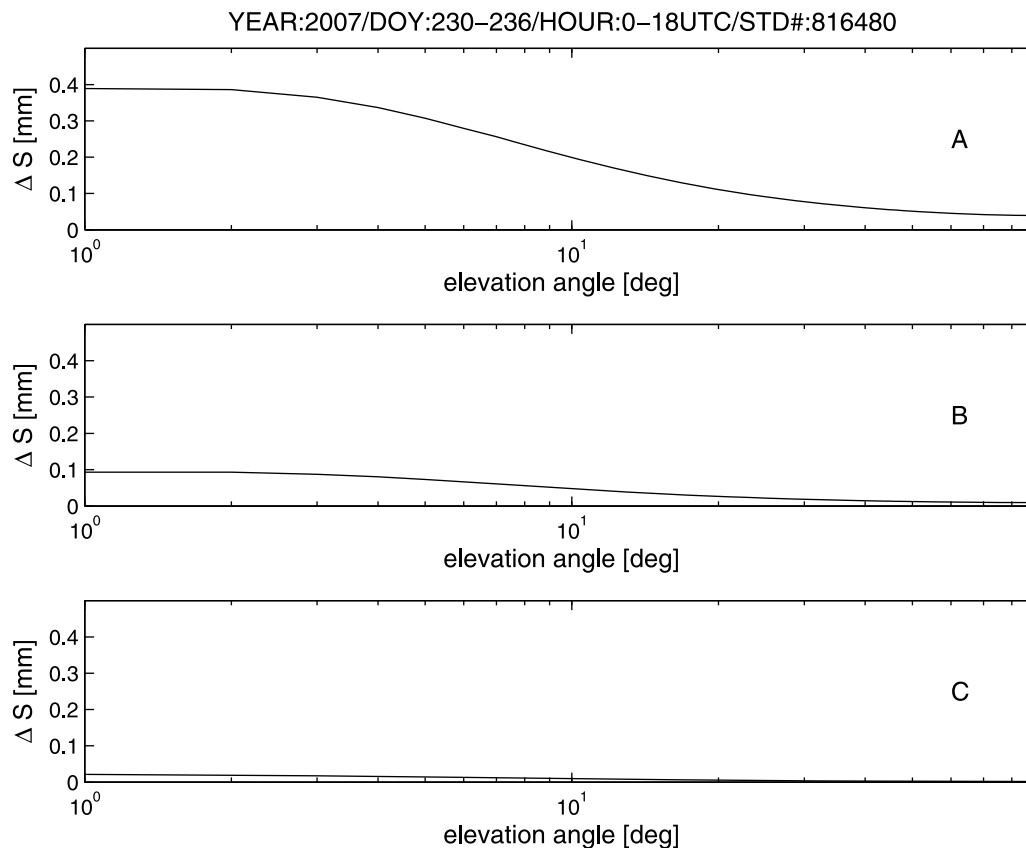


Figure 3. In the STD algorithm the node-sequence is successively refined by node insertion; solution A, B, C and R. The latter serves as the reference solution (for details refer to the text). The root-mean square deviation as a function of the elevation angle for (top) option A, (middle) option B, and (bottom) option C. In total 816480 STDs enter the comparison.

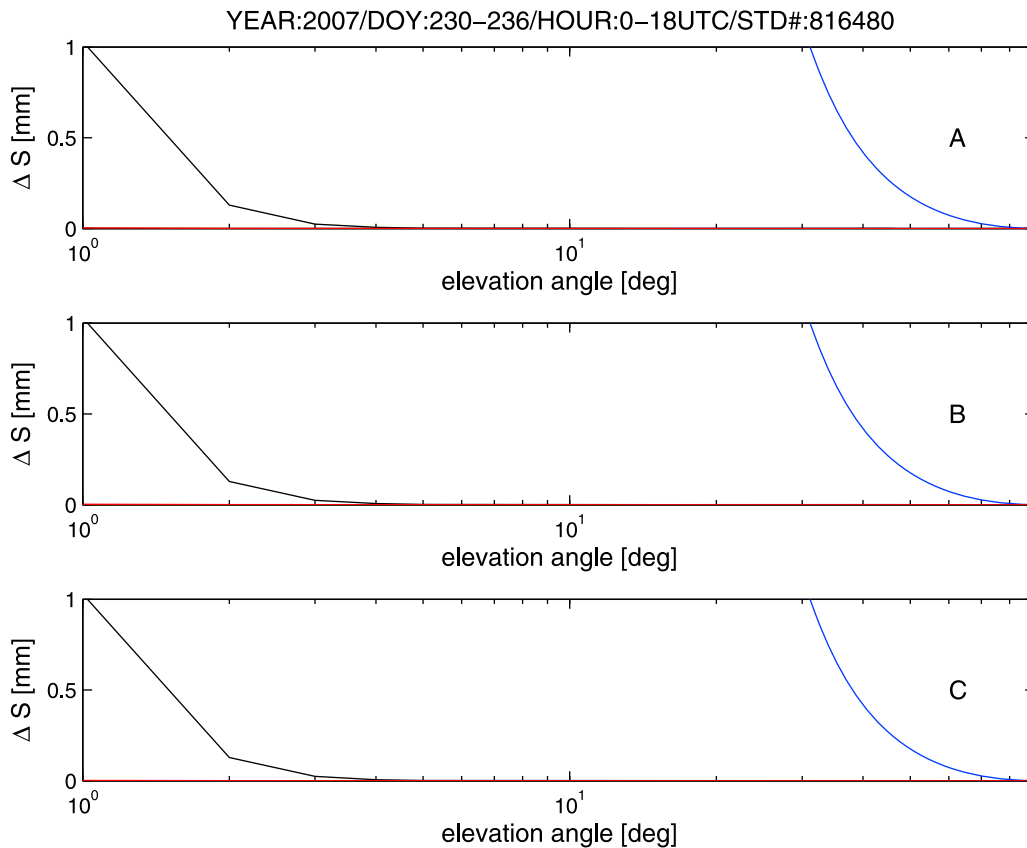


Figure 4. In the STD algorithm the number of iterations in Newton’s method is increased from zero (no iteration) to three. The latter serves as the reference solution (for details refer to the text). The root-mean square deviation as a function of the elevation angle for (top) option A, (middle) option B, and (bottom) option C. The blue, black and red line indicate the root-mean square deviation for zero, one and two iterations in Newton’s method respectively. In total 816480 STDs enter the comparison.

function of the elevation angle. As expected, the root-mean square deviation tends to zero, if the node-sequence is successively refined by node insertion. For any solution A, B or C the root-mean square deviation is <1 mm for the entire elevation range. Next, the number of iterations in Newton’s method is increased from zero (no iteration) to the default value three. For the node-sequence A, B and C, the solutions A, B and C from the previous numerical experiment serve as the reference solutions respectively. Figure 4 shows the root-mean square deviation as a function of the elevation angle. Irrespectively of the node-sequence we observe fast and safe convergence. This can be explained by the fact that the first guess vector used in Newton’s method is an approximate zero. A remarkable feature of the algorithm is obvious; irrespectively of the node-sequence, two iterations in Newton’s method are sufficient for the entire elevation range.

3.2. Computational Efficiency

[27] On an ordinary PC (Core2Quad Intel processor, 2.5 GHz, 2 GB RAM) a few tens of STDs per second are computed using a single core. The data throughput depends on the node-sequence and the number of iterations in Newton’s method. Two approximations enhance the computational efficiency without altering the accuracy significantly; the algorithm is restricted to the plane defined by the center of the Earth, the receiver and the satellite and the

partial derivative of the refractivity with respect to the longitude and latitude at any point is neglected. It is evident that the two approximations increase computational efficiency; the number of equations is reduced by a factor of two, the bandwidth of the Jacobian is reduced from seven to three and the non-zero entries of the Jacobian simplify considerably. The validness of both approximations is shown in the next numerical experiment. For the node-sequence A, B, and C we compute STDs using both approximations (we use three iterations in Newton’s method); in the following referred to as solution A’, B’ and C’. The solution R serves as the reference solution. The main characteristics of the solutions are summarized in Table 1. Figure 5 shows the root-mean square deviation as a function of the elevation angle. Again, for any solution A’, B’ or C’ the root-mean square deviation is <1 mm for the entire elevation range. The non-zero root-mean square deviation is primary due to the different node-sequence and not due to the approximations. In fact, for the same node-sequence and the same number of iterations in Newton’s method, the root-mean square deviation is <0.01 mm for the entire elevation range.

[28] Based on the numerical experiments, the following implementation of the algorithm is proposed: account for the two approximations, use the default node-sequence and use two iterations in Newton’s method. This implementation of the algorithm meets the following criteria: irrespectively of

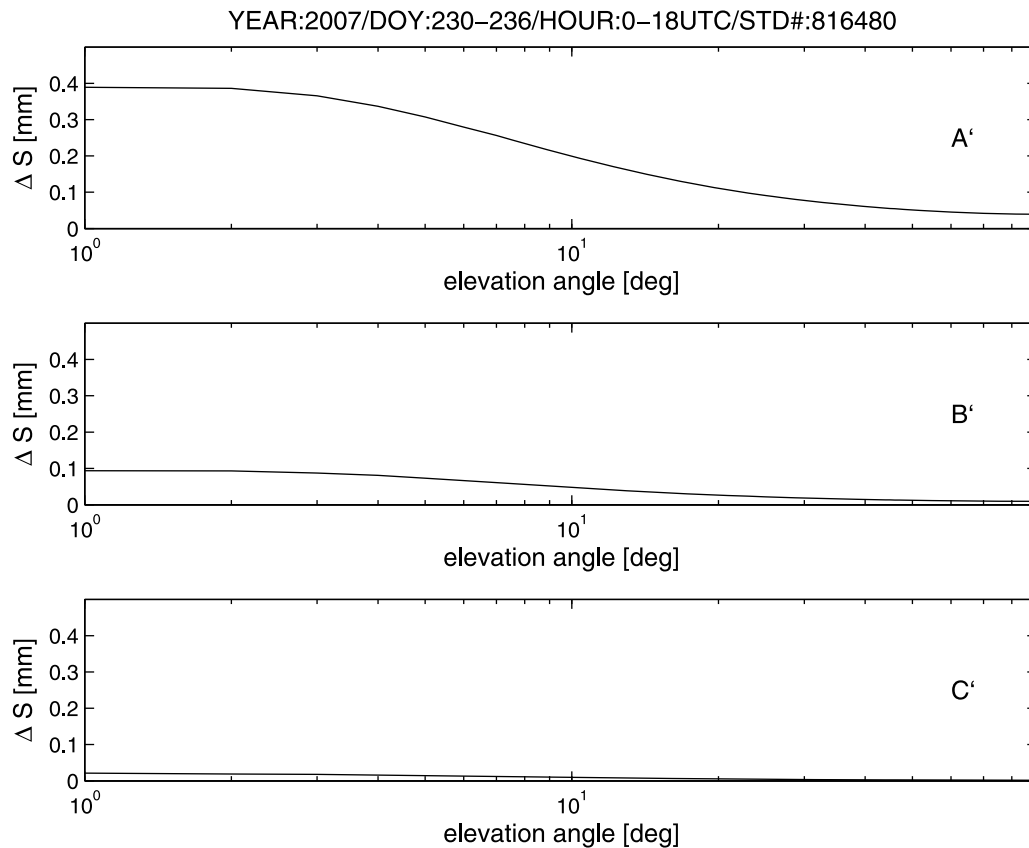


Figure 5. The STD algorithm is restricted to a plane and partial derivatives of the refractivity with respect to the longitude (latitude) at an arbitrary point are neglected. The number of nodes is successively doubled; solution A', B' and C'. The solution R serves as the reference solution (for details refer to the text). The root-mean square deviation as a function of the elevation angle for (top) option A', (middle) option B', and (bottom) option C'. In total 816480 STDs enter the comparison.

the elevation angle the error of STDs is <1 mm and the computational speed is ~ 1000 STDs per second using a single core.

3.3. Uncertainty of STDs

[29] We distinguish between uncertainty of STDs due to simplifying assumptions in the algorithm and uncertainty of STDs due to the uncertainty of the refractivity field.

3.3.1. Uncertainty of STDs Due to Simplifying Assumptions

[30] For better computational efficiency a number of simplifying assumptions were introduced; the Earth is assumed to be a perfect sphere with radius equal to Earth's mean radius of curvature at the center point of the limited area NWM domain, the original NWM refractivity field is re-sampled and the interpolation routine that is used to compute the refractivity at an arbitrary point is simple (see Appendix A). Numerical experiments are carried out to estimate the uncertainties of STDs due to these simplifying assumptions. In the first numerical experiment, the reference coordinate system is not an osculating sphere but the WGS84 (World Geodetic System 1984). We interpret the latitudes (longitudes) of NWM grid points as geodetic latitudes (longitudes) and convert the height above mean sea level of NWM grid points to the height above the reference ellipsoid using the EGM96 (Earth Gravitational Model

1996). In order to highlight differences between the ellipsoid and the osculating sphere, STDs are computed for azimuthal angles 0° – 270° (stepsize 90°). In the second numerical experiment the original NWM refractivity field is not re-sampled and instead of bilinear interpolation, bicubic interpolation [Keys, 1981] with respect to longitude and latitude is performed. In both experiments the solution A' serves as the reference solution. The main characteristics of the solutions are summarized in Table 1. The uncertainty is measured in terms of the mean deviation and the standard deviation from the reference solution. Figure 6 shows the mean deviation and the standard deviation as a function of the elevation angle. In both experiments the standard deviation is larger than the mean deviation. In the first experiment this can be explained by the fact that the radius of curvature of the ellipsoid varies with azimuth while the radius of the osculating sphere is constant. The increased (decreased) radius of curvature of the ellipsoid leads to an increased (decreased) STD. The large standard deviation compared to the small mean deviation in the second experiment can be explained by the fact that differences between bilinear and bicubic interpolation are random and not systematic. Based on the two numerical experiments we estimate that the uncertainty of STDs due to simplifying assumptions in the algorithm is ~ 1 mm in the zenith and ~ 1 cm for an elevation angle of 5° .

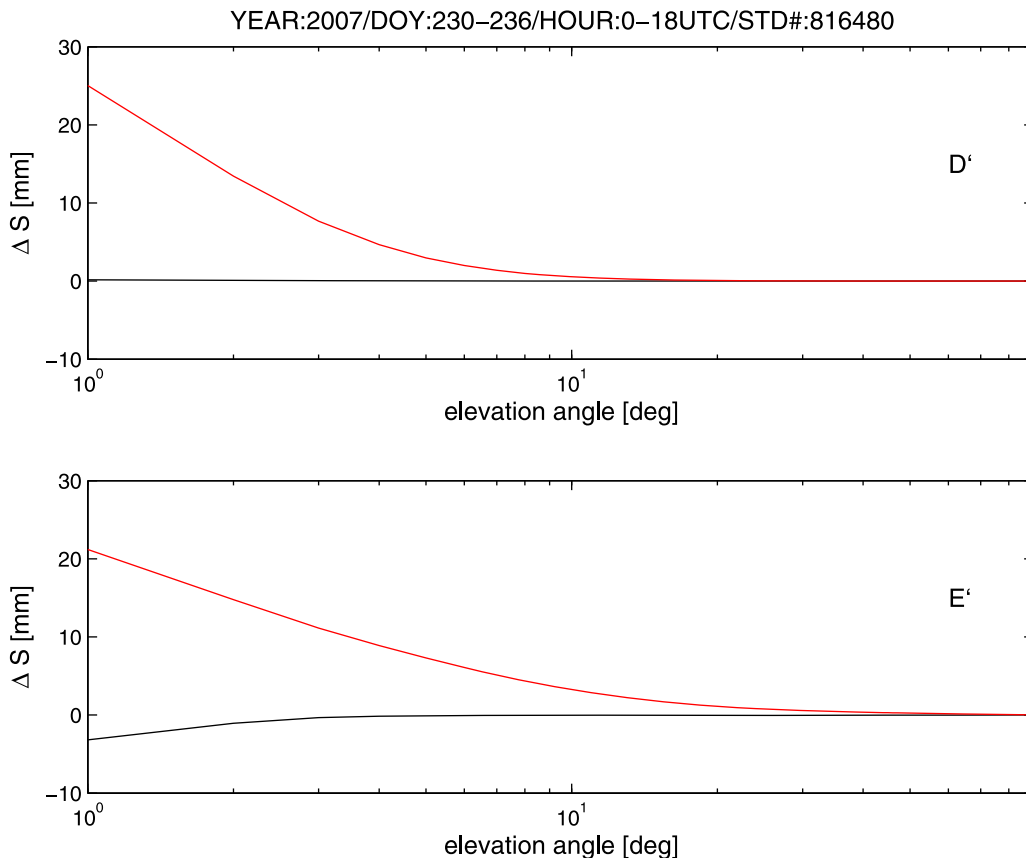


Figure 6. In the STD algorithm the WGS84 is used; solution D'. In the STD algorithm a different interpolation routine for the refractivity is used; solution E'. The solution A' serves as the reference solution (for details refer to the text). (top) The STD deviation versus the elevation angle for option D'. (bottom) The STD deviation versus the elevation angle for option E'. The black line indicates the mean deviation and the red line indicates the standard deviation. In total 816480 STDs enter the comparison.

3.3.2. Uncertainty of STDs Due to the Uncertainty of the Refractivity Field

[31] The ECMWF meteorological variables (pressure, temperature and humidity) contain model errors. Therefore, the refractivity field and subsequently the STDs are uncertain. Let ξ denote the refractivity field and let \mathbf{B} denote the refractivity error covariance matrix. The diagonal elements of the matrix \mathbf{B} store the squared refractivity error variances and the off-diagonal elements of the matrix \mathbf{B} store the refractivity error covariances. The STD error covariance matrix \mathbf{B}' can be determined according to (propagation of uncertainties)

$$\mathbf{B}'[\xi] = \mathbf{S}[\xi] \mathbf{B} \mathbf{S}[\xi]^T. \quad (23)$$

[32] The diagonal elements of the matrix \mathbf{B}' store the squared STD error variances and the off-diagonal elements of the matrix \mathbf{B}' store the STD error covariances. The tangent-linear operator of the algorithm \mathbf{S} is given through

$$\mathbf{S} = \frac{\partial \mathbf{S}}{\partial \xi} \quad (24)$$

and is constructed by rigorous application of the chain rule of differential calculus on a coding level [Giering and

Kaminski, 1998]. If the ECMWF analysis error covariance matrix (the analysis error covariance matrix stores the uncertainty of the meteorological variables) is accessible, the refractivity error covariance matrix and the STD error covariance matrix can be computed.

[33] The ECMWF analysis error covariance matrix is not accessible at the GFZ. Therefore, a rough estimate of the uncertainty of STDs due to uncertainty of the refractivity field is provided as follows. At first, we assume that in the vicinity of a ground-based receiver the refractivity N is a function of height h only, i.e. $N = N(h)$. Second, the refractivity error variance in percent p as a function of height h is assumed to be of the form [Steiner et al., 2006]

$$p(h) = p_f + \frac{p_{f+1} - p_f}{l_{f+1} - l_f} (h - l_f) \quad h \in [l_f, l_{f+1}) \quad (25)$$

with $p = p_{f+1}$ for $h \geq l_{f+1}$. Significant heights are defined as $l_0 = 0$ km, $l_1 = 8$ km, $l_2 = 25$ km and $l_3 = 60$ km. Significant refractivity error variances in percent are estimated from Steiner et al. [2006] to be $p_0 = 2\%$, $p_1 = 0.5\%$, $p_2 = 0.5\%$ and $p_3 = 1\%$. This estimate does not take into account any hourly, daily, seasonal or geographical dependency. Third,

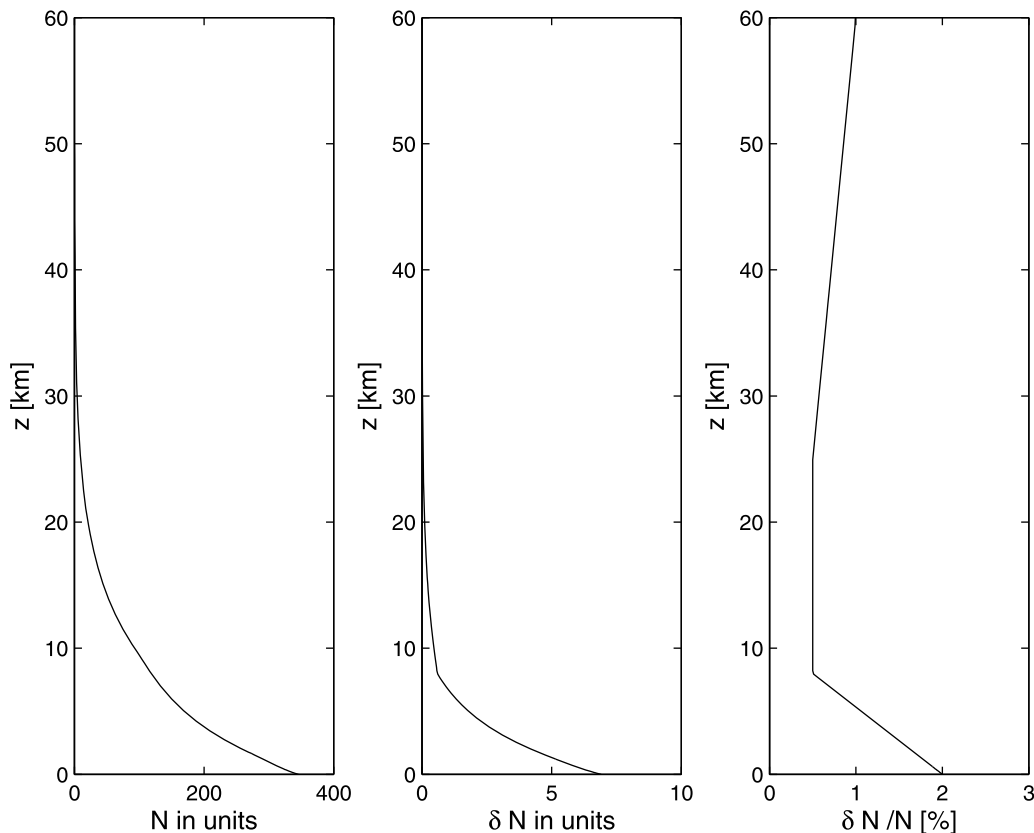


Figure 7. (left) The refractivity as a function of the height. The refractivity profile corresponds to the mean refractivity profile (averaged over the limited area ECMWF model domain) valid at 12 UTC for the DOY 234 in the year 2007. (middle) The estimated refractivity error variance as a function of the height. (right) The estimated fractional refractivity error variance as a function of the height (for details refer to the text).

the refractivity error covariance matrix is assumed to be of the form [Rodgers, 1990]

$$B_{ij} = p(h_i)p(h_j)N(h_i)N(h_j) \exp(-(h_i - h_j)^2 \zeta^{-2}) \quad (26)$$

where h_i and h_j stand for the i th and j th model height respectively and ζ denotes the error correlation length. We set $\zeta = 0$ m or alternatively $\zeta = 500$ m.

[34] Figure 7 shows a refractivity profile and the refractivity error variance profile. The refractivity profile corresponds to the mean refractivity profile (averaged over the limited area ECMWF model domain) valid at 12 UTC for the DOY 234 in the year 2007. A hypothetical ground based receiver is located at mean sea level. STDs and STD error variances are computed for elevation angles 1° – 90° (stepsize 1°). Figure 8 shows the STD and the STD error variance as a function of the elevation angle. The STD error variance largely depends on the error correlation length ζ . If $\zeta = 0$ m, the STD error variance is ~ 3 mm in the zenith and ~ 3 cm for an elevation angle of 5° . If $\zeta = 500$ m, the STD error variance is ~ 8 mm in the zenith and ~ 8 cm for an elevation angle of 5° . For both options, the fractional STD error variance is almost independent of the elevation angle.

[35] Without detailed knowledge of the ECMWF analysis error covariance matrix, in particular detailed knowledge of error correlations, it is difficult to estimate the uncertainty of STDs due to uncertainty of the refractivity field. However, our estimates indicate that the uncertainty of STDs due to uncertainty of the refractivity field is significantly larger than the uncertainty of STDs due to simplifications in the algorithm. If we sum up the uncertainty of STDs due to the uncertainty of the refractivity field and the uncertainty of STDs due to simplifications in the algorithm we estimate the uncertainty of STDs derived from the ECMWF analysis to be ~ 4 – 9 mm in the zenith and ~ 4 – 9 cm for an elevation angle of 5° . Though this estimate must be regarded as rough it is in good agreement with the estimate provided by Järvinen *et al.* [2007], who conclude that the uncertainty of STDs derived from the High-Resolution Limited-Area Model is ~ 8 mm in the zenith and ~ 8 cm for an elevation angle of 5° .

4. Application

[36] The algorithm is implemented in an OpenMP environment. The number of computed STDs per second scales about linearly with the number of cores. Monitoring of STD

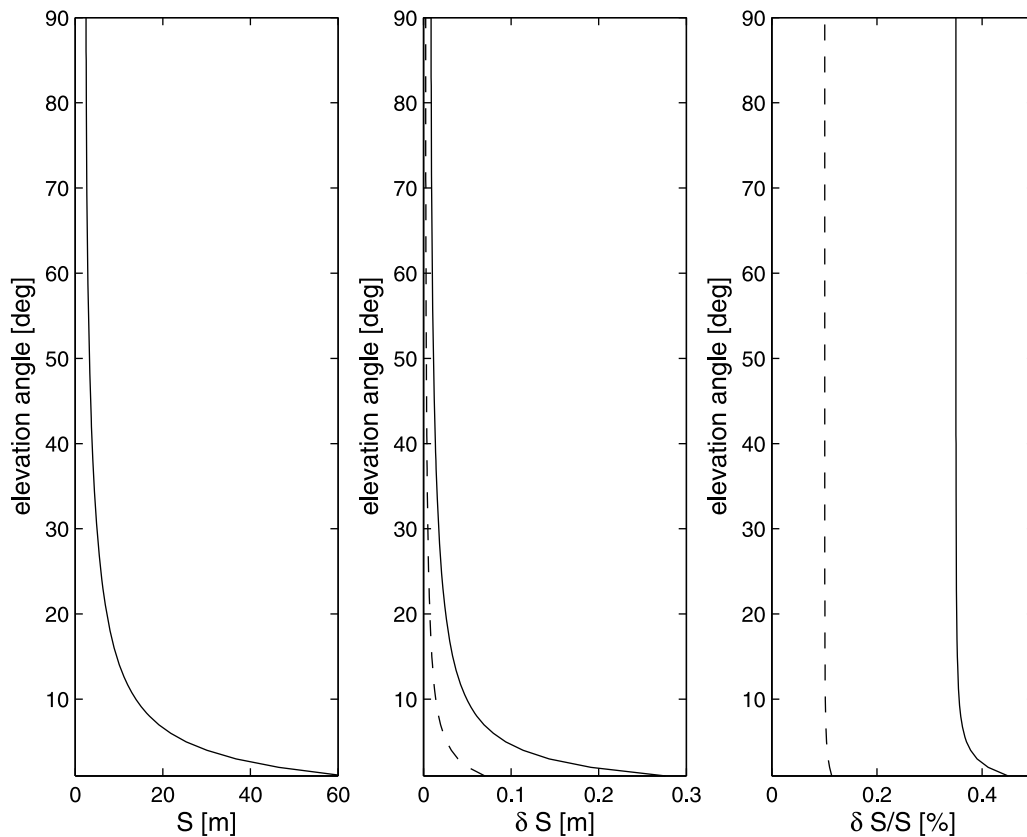


Figure 8. (left) The STD as a function of the elevation angle. (middle) The STD error variance as a function of the elevation angle. (right) The fractional STD error variance as a function of the elevation angle. The STD and the STD error variance are computed using the refractivity and refractivity error variance shown in the previous figure. The dashed line corresponds to the case of an error correlation length $\zeta = 0$ m, and the solid line corresponds to an error correlation length $\zeta = 500$ m (for details refer to the text).

data processed for a large and continuously operating network of receivers against STDs derived from ECMWF analyses is efficiently possible. In the following STDs retrieved from GPS phase-observations will be referred to as GFZ STDs and STDs derived from the ECMWF analyses will be referred to as ECMWF STDs.

4.1. GPS Data Processing at the GFZ

[37] The EPOS (Earth Parameter and Orbit determination System) software developed at the GFZ is used to retrieve ZTDs (Zenith Total Delays) and STDs from GPS phase-observations [Gendt *et al.*, 2004]. ZTDs and STDs are provided for about 300 stations in Germany. Zero-differenced observations with an elevation cut-off angle of 7° are processed in precise point positioning mode [Zumberge *et al.*, 1997]. Precise satellite orbits and clocks as well as earth rotation parameters are available from the IGS (International GNSS Service) analysis center at the GFZ. Atmospheric parameters are estimated in a least-square adjustment. The ZTDs are estimated using all satellite-receiver links available within 15 minutes. STDs are reconstructed for each satellite-receiver link and are available every 150 s. Specifically, let ϵ and φ denote the elevation and azimuth of the satellite-

receiver link and let ZHD and ZWD denote the zenith hydrostatic and wet delay [Davis *et al.*, 1985], then the STD is reconstructed according to

$$S = m_h(\epsilon)ZHD + m_w(\epsilon)[ZWD + \cot(\epsilon)(G_N \cos(\varphi) + G_E \sin(\varphi))] + P_R \quad (27)$$

where m_h and m_w denote the hydrostatic and wet mapping function [Niell, 1996], G_N and G_E denote the gradients in north and east direction [Davis *et al.*, 1993] and P_R denotes the postfit residual. The zenith hydrostatic delay is estimated using the pressure at the receiver site [Davis *et al.*, 1985]. The gradients in north and east direction are estimated once per hour. The impact of different mapping functions on estimated zenith delays is subject to numerous studies. Though we can not provide an estimate of the uncertainty of ZTDs due to the mapping function in our GNSS analysis, we can anticipate that this uncertainty of ZTDs is ~ 1 – 2 mm for a receiver located in Germany (see e.g. IERS Annual Report 2006 available online at <http://www.iers.org>). For the following statistical comparison it is also important to note that ZTDs or STDs are not assimilated at the ECMWF.

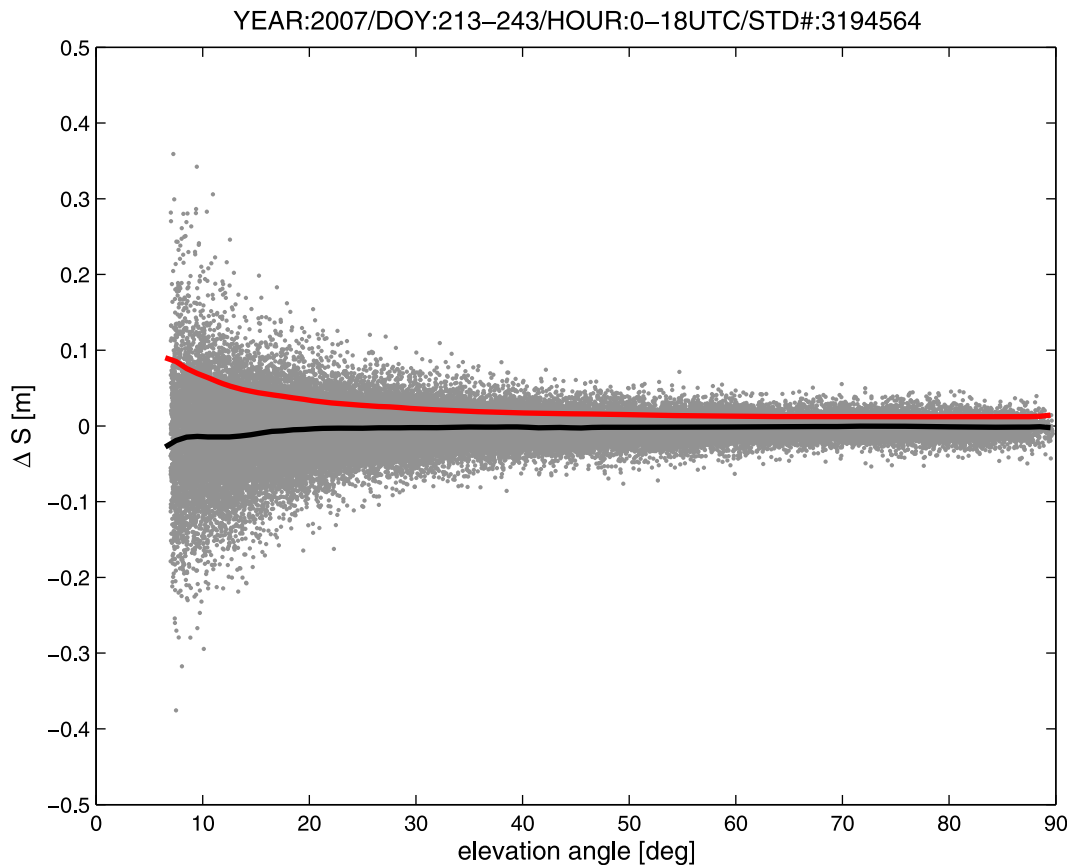


Figure 9. The deviation between GFZ STDs and ECMWF STDs as a function of the elevation angle. The black line indicates the mean deviation and the red line indicates the standard deviation. The grey dots represent individual STD differences. In total 3194564 STDs enter the comparison.

4.2. Statistical Comparison

[38] The focus is on DOY 213–243 (August) in the year 2007. STDs are assembled from a network of 270 receivers in Germany. The location of the receivers is shown in Figure 2. ECMWF analyses are available at 0, 6, 12 and 18 UTC. STDs within a time window of 15 minutes around the ECMWF analysis time enter the comparison. The discrepancy between STDs is measured in terms of the STD deviation $\Delta S = S_G - S$. Here S_G denote GFZ and S denote ECMWF STDs. Figure 9 shows the STD deviation as a function of the elevation angle. Figure 10 (top) shows the fractional STD deviation as a function of the elevation angle and Figure 10 (bottom) shows the fractional number of STDs as a function of the elevation angle. While the STD deviation increases with decreasing elevation angles, the fractional STD deviation is about constant. A possible explanation for the enhanced negative bias at 7° is signal multipath contained in GFZ STDs. The fractional standard deviation is 0.48% and the fractional mean deviation is -0.06% . With a mean ZTD of 2.4 m, this corresponds to a standard deviation of 12 mm and a mean deviation of -1 mm close to the zenith. The STD deviation is a composite of ECMWF and GFZ STD errors. Under the assumption that error distributions are Gaussian with zero mean and independent, the standard deviation σ is related to the error variance of ECMWF STDs σ_E and the error

variance of GFZ STDs σ_G according to $\sigma^2 = \sigma_E^2 + \sigma_G^2$. Our estimate of the uncertainty of ECMWF STDs close to the zenith ~ 4 – 9 mm indicates that the uncertainty of GFZ STDs close to the zenith is ~ 8 – 11 mm. In essence, the quality of STDs derived from GPS-phase observations is comparable to the quality of STDs derived from the ECMWF analysis. Figure 11 (top) shows the fractional STD deviation for individual days and Figure 11 (bottom) shows the fractional number of STDs for individual days. In contrast to the fractional STD deviation as a function the elevation angle, the fractional STD deviation as a function of the time exhibits a large variability. The quality of ECMWF STDs depends on the actual state of the atmosphere. Whether the quality of GFZ STDs depends on the actual state of the atmosphere is not known. In any case, a possible explanation for the increased fractional mean and standard deviation on particular days are severe weather phenomena. In general, these results are consistent with results obtained from a comparable study [Pany *et al.*, 2001].

[39] Next, ZTDs retrieved from GPS phase-observations (GFZ ZTDs) are compared with ZTDs derived from the ECMWF analyses (ECMWF ZTDs). The comparison is carried out for the same time period. The discrepancy between ZTDs is measured in terms of the ZTD deviation $\Delta Z = Z_G - Z$, where Z_G denote GFZ and Z denote ECMWF ZTDs. The fractional standard deviation is 0.44% and the

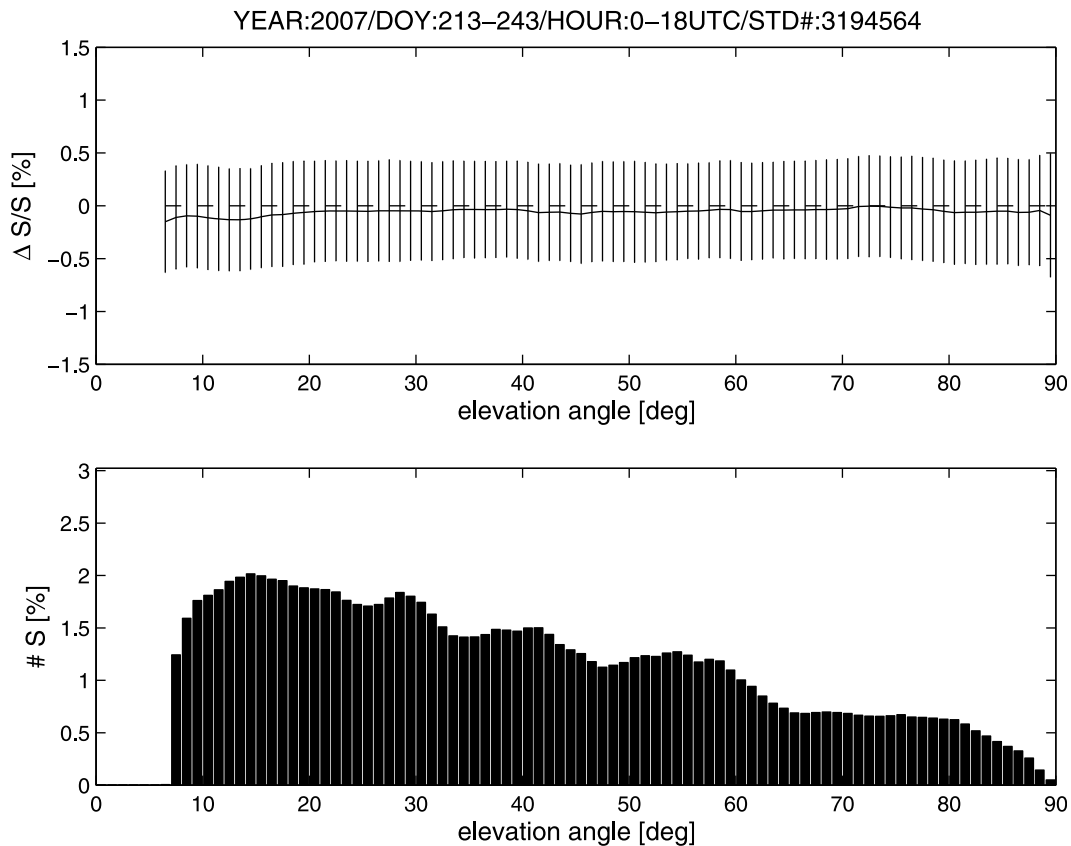


Figure 10. (top) The fractional deviation between GFZ STDs and ECMWF STDs as a function of the elevation angle. The black line indicates the mean deviation and the error bars indicate the \pm one-sigma deviation from the mean deviation. (bottom) The fractional number of STDs as a function of the elevation angle. In total 3194564 STDs enter the comparison.

fractional mean deviation is -0.06% . With a mean ZTD of 2.4 m, this corresponds to a standard deviation of 11 mm and a mean deviation of -1 mm. Our estimate of the uncertainty of ECMWF ZTDs ~ 4 – 9 mm indicates that the uncertainty of GFZ ZTDs is ~ 6 – 10 mm. Figure 12 (top) shows the fractional ZTD deviation for individual days and Figure 12 (bottom) shows the fractional number of ZTDs for individual days. Similar to the fractional STD deviation as a function of the time, the fractional ZTD deviation as a function of the time exhibits a large variability. The comparison indicates that GFZ STD data quality is comparable to GFZ ZTD data quality. The fractional STD standard deviation is somewhat larger than the fractional ZTD standard deviation. A possible explanation is more noise contained in GFZ STDs compared to GFZ ZTDs.

5. Conclusion

[40] An algorithm was developed to compute STDs using the refractivity field of a NWM. The ray-trajectory equation is solved using an implicit finite difference scheme. The location of the ground-based receiver and the satellite is automatically part of the solution. The structured non-linear system of equations, arising due to the implicit finite difference scheme, is solved by Newton's method. In a series of numerical experiments the accuracy and the computational

speed of the algorithm are estimated. The implementation of the algorithm meets the following criteria: irrespectively of the elevation angle the error of STDs is < 1 mm and the computational speed is ~ 1000 STDs per second using a single core. It is important to note that the estimates for the accuracy and the computational speed of the algorithm are based on refractivity fields derived from a NWM with relative low horizontal resolution; the horizontal resolution of the ECMWF analysis used in this study is $0.5^\circ \times 0.5^\circ$. Whether these estimates hold true for refractivity fields derived from different NWMs, in particular those with increased horizontal resolution, will be assessed in a future study.

[41] We experimented with different interpolation routines and different radii of the Earth to estimate the uncertainty of STDs due to simplifying assumptions in the algorithm. Since the ECMWF analysis error covariance matrix and hence the refractivity error covariance matrix is not accessible a model refractivity error covariance matrix is used to estimate the uncertainty of STDs due to the uncertainty of the refractivity field. Though, our estimates must be regarded as rough, they indicate that the uncertainty of STDs due to uncertainty in the refractivity field is larger than the uncertainty of STDs due to simplifying assumptions in the algorithm. Combining our estimates we conclude that, the uncertainty of STDs derived from the ECMWF analysis is on a sub-centimeter

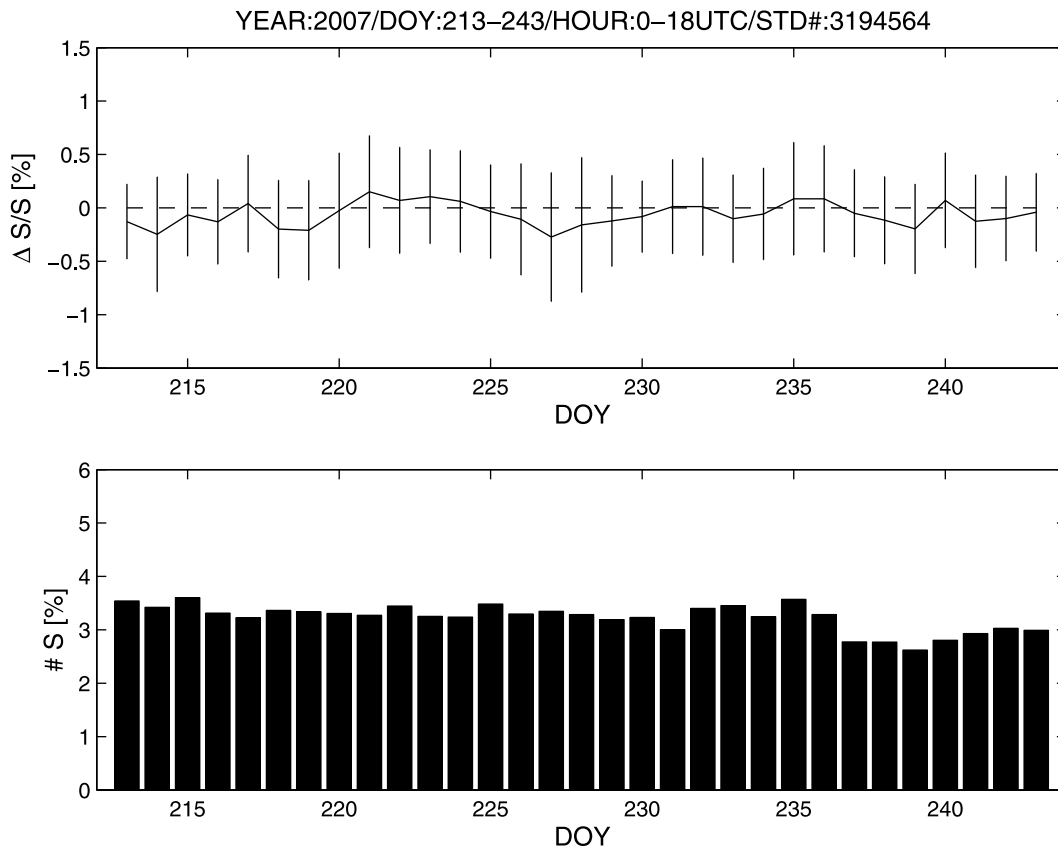


Figure 11. (top) The fractional deviation between GFZ STDs and ECMWF STDs as a function of the day of year. The black line indicates the mean deviation and the error bars indicate the \pm one-sigma deviation from the mean deviation. (bottom) The fractional number of STDs as a function of the day of year. In total 3194564 STDs enter the comparison.

level in the zenith and on a sub-decimeter level for an elevation angle of 5° . This estimate does not take into account the uncertainty of the empirically determined constants relating refractivity to pressure, temperature and humidity [Aparicio and Laroche, 2011].

[42] In this study, we compare STDs retrieved from GPS phase-observations with STDs derived from the ECMWF analysis. The statistical comparison for a large and continuously operating network of ground-based receivers in Germany indicates good agreement; in August 2007 the random deviation is 0.5% and the systematic deviation is 0.1%. These values are consistent with values obtained in a comparable study [Pany *et al.*, 2001].

[43] There are a number of potential applications for the proposed algorithm. For example, having developed a fast and accurate method to compute STDs using the refractivity field of a NWM (the forward code), we can construct the tangent-linear and adjoint code for variational data analysis. The technical description of these codes along with simulation studies is subject to a follow-up work.

Appendix A

[44] The ECMWF meteorological fields are provided with a horizontal resolution of $0.5^\circ \times 0.5^\circ$ on 91 model levels

extending from Earth's surface to 80 km. The pressure, the temperature and the specific humidity are stored at grid points, specified by longitude, latitude and height above mean sea level.

[45] At first, the refractivity is computed at each grid point in the NWM domain. Hereinafter, the one dimensional arrays Ψ_I and Φ_J with $I = 1, \dots, M_I$ and $J = 1, \dots, M_J$ denote the horizontal grid point coordinates of the model grid. The integers M_I and M_J denote the horizontal dimensions of the model grid. The three dimensional arrays H_{IJK} and N_{IJK} for $I = 1, \dots, M_I, J = 1, \dots, M_J$ and $K = 1, \dots, M_K$ store the model height and the model refractivity respectively. The integer M_K denotes the vertical dimension of the model grid. To compute the refractivity at an arbitrary point $N(x, y, z)$ a coordinate transformation routine and an interpolation routine is needed. The coordinate transformation routine consists of transforming cartesian coordinates (x, y, z) to spherical coordinates (φ, ϕ, h) . Here φ denotes the longitude, ϕ denotes the latitude and h denotes the height. The interpolation routine consists of the following steps:

[46] Step a) Determine the neighboring grid point indices I and J and compute the increments X and Y :

$$\begin{aligned} X &= (\varphi - \Psi_I) \cdot (\Psi_{I+1} - \Psi_I)^{-1} \\ Y &= (\phi - \Phi_J) \cdot (\Phi_{J+1} - \Phi_J)^{-1}. \end{aligned} \quad (\text{A1})$$

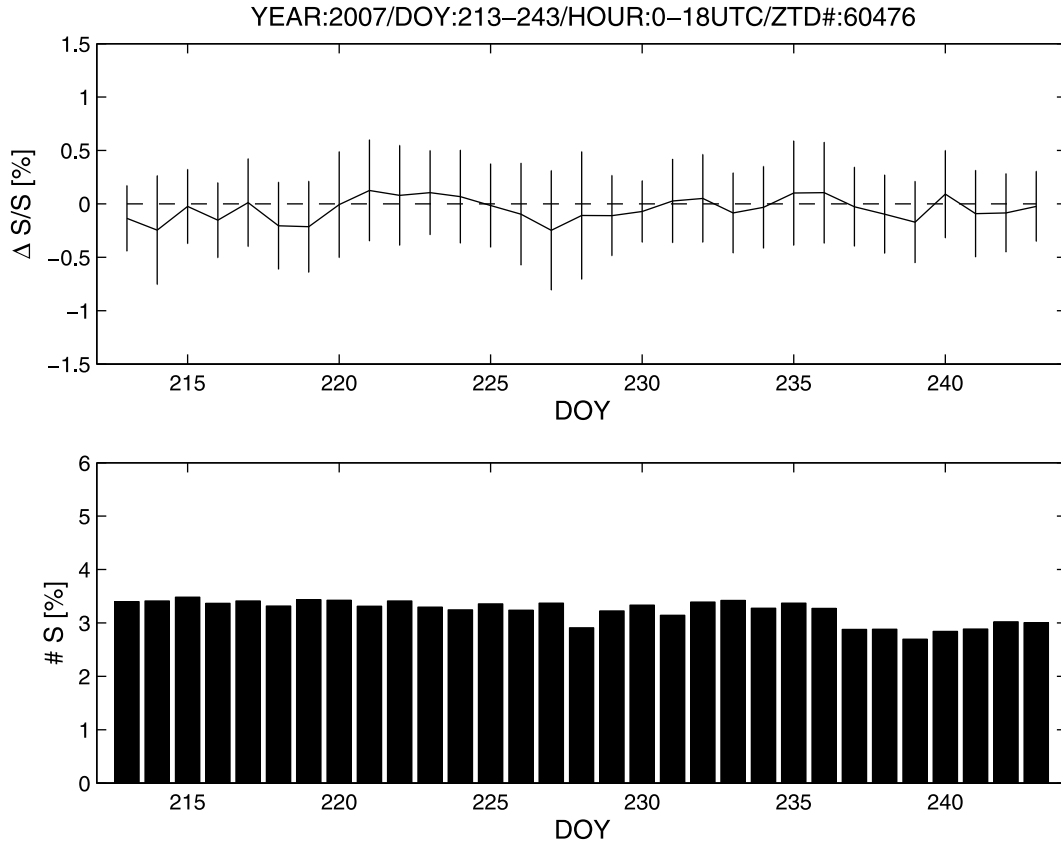


Figure 12. (top) The fractional deviation between GFZ ZTDs and ECMWF ZTDs as a function of the day of year. The black line indicates the mean deviation and the error bars indicate the \pm one-sigma deviation from the mean deviation. (bottom) The fractional number of ZTDs as a function of the day of year. In total 60476 ZTDs enter the comparison.

[47] Step b) Compute the bilinear interpolation coefficients X_1, X_2, X_3, X_4 :

$$\begin{aligned} X_1 &= (1 - X) \cdot (1 - Y) \\ X_2 &= (1 - X) \cdot Y \\ X_3 &= X \cdot (1 - Y) \\ X_4 &= X \cdot Y \end{aligned} \quad (\text{A2})$$

[48] Step c) Determine at the neighboring grid points the adjacent grid point indices with respect to height A, B, C, D by binary search and compute the vertical interpolation coefficients L_1, L_2, L_3, L_4 :

$$\begin{aligned} L_1 &= (h - H_{IJ}) \cdot (H_{IJ} - H_{IJ-1})^{-1} \\ L_2 &= (h - H_{IJ+1B}) \cdot (H_{IJ+1B} - H_{IJ+1B-1})^{-1} \\ L_3 &= (h - H_{I+1JC}) \cdot (H_{I+1JC} - H_{I+1JC-1})^{-1} \\ L_4 &= (h - H_{I+1J+1D}) \cdot (H_{I+1J+1D} - H_{I+1J+1D-1})^{-1} \end{aligned} \quad (\text{A3})$$

[49] Step d) Perform logarithmic interpolation to compute the refractivity values N_1, N_2, N_3, N_4 :

$$\begin{aligned} N_1 &= N_{IJ} \cdot (N_{IJ} \cdot N_{IJ-1}^{-1})^{L_1} \\ N_2 &= N_{IJ+1B} \cdot (N_{IJ+1B} \cdot N_{IJ+1B-1}^{-1})^{L_2} \\ N_3 &= N_{I+1JC} \cdot (N_{I+1JC} \cdot N_{I+1JC-1}^{-1})^{L_3} \\ N_4 &= N_{I+1J+1D} \cdot (N_{I+1J+1D} \cdot N_{I+1J+1D-1}^{-1})^{L_4} \end{aligned} \quad (\text{A4})$$

[50] Step e) Compute the refractivity N :

$$N = \sum_{l=1}^4 X_l \cdot N_l \quad (\text{A5})$$

[51] Above/below the NWM top/bottom log-linear extrapolation is performed. Beyond NWM lateral boundaries the nearest refractivity profile is used.

[52] The computation of the partial derivative of N with respect to x, y or z is performed by rigorous application of the chain rule of differential calculus. For reasons of clarity and comprehensibility we provide the computations in the interpolation routine in detail. The computations in the coordinate transformation routine are carried out in a similar manner. Hereinafter the subscript ξ denotes the partial derivative with respect to x, y or z :

[53] Step a) reads as:

$$\begin{aligned} X_{\xi} &= \varphi_{\xi} \cdot (\Psi_{J+1} - \Psi_J)^{-1} \\ Y_{\xi} &= \phi_{\xi} \cdot (\Phi_{J+1} - \Phi_J)^{-1} \end{aligned} \quad (\text{A6})$$

[54] Step b) reads as:

$$\begin{aligned} X_{1,\xi} &= -X_{\xi} \cdot (1 - Y) - (1 - X) \cdot Y_{\xi} \\ X_{2,\xi} &= -X_{\xi} \cdot Y + (1 - X) \cdot Y_{\xi} \\ X_{3,\xi} &= X_{\xi} \cdot (1 - Y) - X \cdot Y_{\xi} \\ X_{4,\xi} &= X_{\xi} \cdot Y + X \cdot Y_{\xi} \end{aligned} \quad (\text{A7})$$

[55] Step c) reads as:

$$\begin{aligned} L_{1,\xi} &= h_\xi \cdot (H_{IJA} - H_{IJA-1})^{-1} \\ L_{2,\xi} &= h_\xi \cdot (H_{IJ+1B} - H_{IJ+1B-1})^{-1} \\ L_{3,\xi} &= h_\xi \cdot (H_{I+1JC} - H_{I+1JC-1})^{-1} \\ L_{4,\xi} &= h_\xi \cdot (H_{I+1J+1D} - H_{I+1J+1D-1})^{-1} \end{aligned} \quad (A8)$$

[56] Step d) reads as:

$$\begin{aligned} N_{1,\xi} &= N_1 \cdot \log(N_{IJA} \cdot N_{IJA-1}^{-1}) \cdot L_{1,\xi} \\ N_{2,\xi} &= N_2 \cdot \log(N_{IJ+1B} \cdot N_{IJ+1B-1}^{-1}) \cdot L_{2,\xi} \\ N_{3,\xi} &= N_3 \cdot \log(N_{I+1JC} \cdot N_{I+1JC-1}^{-1}) \cdot L_{3,\xi} \\ N_{4,\xi} &= N_4 \cdot \log(N_{I+1J+1D} \cdot N_{I+1J+1D-1}^{-1}) \cdot L_{4,\xi} \end{aligned} \quad (A9)$$

[57] Step e) reads as:

$$N_\xi = \sum_{l=1}^4 (X_{l,\xi} \cdot N_l + X_l \cdot N_{l,\xi}) \quad (A10)$$

[58] For better computational efficiency a user specific grid is defined where the model height satisfies $\hat{H}_{IL} = \hat{H}_L$ for $I = 1, \dots, M_I$, $J = 1, \dots, M_J$ and $L = 0, \dots, F$. For an arbitrary point in the user specific grid $\hat{A} = \hat{B} = \hat{C} = \hat{D}$ and $\hat{L}_1 = \hat{L}_2 = \hat{L}_3 = \hat{L}_4$. The refractivity at each grid point of the user specific grid is determined using the coordinate transformation and interpolation routine outlined above. In order to circumvent the binary search the user specific grid is defined such that a simple invertible relation exists between the height and the grid point index with respect to height. Since the refractivity tends to decrease exponentially with height, we propose the following ansatz

$$\hat{H}_L = T \frac{\exp(\tau)^{\frac{L}{F}} - 1}{\exp(\tau) - 1} \quad (A11)$$

for $L = 0, \dots, F$. The integer F denotes the vertical dimension, τ denotes the lapse rate and T denotes the top height of the user specific grid. Specifically, for the ECMWF grid we set $F = 200$, $\tau = 6$ and $T = 80$ km. On the uncertainty of STDs due to the interpolation routine the reader is referred to section 3.

[59] **Acknowledgments.** The European Centre of Medium-Range Weather Forecasts provided meteorological analysis fields.

References

Aparicio, J. M., and S. Laroche (2011), An evaluation of the expression of the atmospheric refractivity for GPS signals, *J. Geophys. Res.*, *116*, D11104, doi:10.1029/2010JD015214.

Bender, M., G. Dick, M. Ge, Z. Deng, J. Wickert, H. G. Kahle, A. Raabe, and G. Tetzlaff (2010), Development of a GNSS water vapour tomography system using algebraic reconstruction techniques, *Adv. Space Res.*, *47*, 1704–1720, doi:10.1016/j.asr.2010.05.034.

Bevis, M., S. Businger, T. A. Herring, C. Rocken, R. A. Anthes, and R. Ware (1992), GPS meteorology: Remote sensing of atmospheric water vapor using the Global Positioning System, *J. Geophys. Res.*, *97*, 15,787–15,801.

Bevis, M., S. Businger, T. A. Herring, C. Rocken, R. A. Anthes, and R. Ware (1994), GPS meteorology: Mapping zenith wet delays onto precipitable water, *J. Appl. Meteorol.*, *33*, 379–386.

Boehm, J., B. Werl, and H. Schuh (2006), Troposphere mapping functions for GPS and very long baseline interferometry from European Centre for Medium-Range Weather Forecasts operational analysis data, *J. Geophys. Res.*, *111*, B02406, doi:10.1029/2005JB003629.

Davis, J. L., T. A. Herring, I. I. Shapiro, A. E. Rogers, and G. Elgered (1985), Geodesy by radio interferometry: Effects of the atmospheric modelling errors on estimates of baseline length, *Radio Sci.*, *20*, 1593–1607.

Davis, J. L., G. Elgered, A. E. Niell, and C. E. Kuehn (1993), Ground-based measurement of gradients in the “wet” radio refractivity of air, *Radio Sci.*, *28*(6), 1003–1018.

Gendt, G., G. Dick, C. Reigber, M. Tomassini, Y. Lui, and M. Ramatschi (2004), Near real time GPS water vapor monitoring for numerical weather prediction in Germany, *J. Meteorol. Soc. Jpn.*, *82*, 361–370.

Giering, R., and T. Kaminski (1998), Recipes for adjoint code construction, *ACM Trans. Math. Software*, *24*, 437–474.

Hobiger, T., R. Ichikawa, Y. Koyama, and T. Kondo (2008), Fast and accurate ray-tracing algorithms for real-time space geodetic applications using numerical weather models, *J. Geophys. Res.*, *113*, D20302, doi:10.1029/2008JD010503.

Hofmann-Wellenhof, B., H. Lichtenegger, and J. Collins (1992), *GPS: Theory and Practice*, Springer, New York.

Järvinen, H., R. Eresmaa, H. Vedel, K. Salonen, S. Niemela, and J. de Vries (2007), A variational data assimilation system for ground-based GPS slant delays, *Q. J. R. Meteorol. Soc.*, *133*, 969–980, doi:10.1002/qj.79.

Keys, R. (1981), Cubic convolution interpolation for digital processing, *Acoust. Speech Signal Process.*, *29*, 1153–1160.

Mendes, V. B. (1999), Modeling the neutral-atmosphere propagation delay in radiometric space techniques, PhD thesis, Dep. of Geod. and Geomatics Eng., Univ. of N. B., Fredericton, N. B., Canada.

Niell, A. E. (1996), Global mapping functions for the atmosphere delay at radio wavelengths, *J. Geophys. Res.*, *101*, 3227–3246.

Nievinski, F. G. (2009), Ray-tracing options to mitigate the neutral atmosphere delay in GPS, M.Sc.E. thesis, Dep. of Geod. and Geomatics Eng., Univ. of N. B., Fredericton, N. B., Canada.

Pany, T. (2002), Development and application of tropospheric GPS slant delay models based on numerical weather prediction models and turbulence theory, PhD thesis, Inst. of Eng. Geod. and Meas. Syst., Graz Univ. of Technol., Graz, Austria.

Pany, T., P. Pesec, and G. Stangl (2001), Atmospheric GPS slant path delays and ray tracing through numerical weather models, a comparison, *Phys. Chem. Earth*, *26*, 183–188, doi:10.1016/S1464-1895(01)00044-8.

Rocken, C., S. Sokolovskiy, J. M. Johnson, and D. Hunt (2001), Improved mapping of tropospheric delays, *J. Atmos. Oceanic Technol.*, *18*, 1205–1213.

Rodgers, C. D. (1990), Characterization and error analysis of profiles retrieved from remote sounding measurements, *J. Geophys. Res.*, *95*, 5587–5595.

Steiner, A. K., A. Löscher, and G. Kirchengast (2006), Error characteristics of refractivity profiles retrieved from CHAMP radio occultation data, in *Atmosphere and Climate: Studies by Occultation Methods*, edited by U. Foelsche, G. Kirchengast, and A. K. Steiner, pp. 27–36, Springer, Berlin.

Thayer, G. D. (1974), An improved equation for the radio refractive index of air, *Radio Sci.*, *9*, 803–807.

Zumberge, J. F., M. B. Heflin, D. C. Jefferson, M. M. Watkins, and F. H. Webb (1997), Precise point positioning for the efficient and robust analysis of GPS data from large networks, *J. Geophys. Res.*, *102*, 5005–5018.

M. Bender, Z. Deng, G. Dick, S. Heise, M. Shang-Guan, J. Wickert, and F. Zus, GPS/GALILEO Earth Observation, Helmholtz Centre Potsdam, German Research Centre for Geosciences, Telegrafenberg, D-14473, Potsdam, Germany. (bender@gfz-potsdam.de; deng@gfz-potsdam.de; dick@gfz-potsdam.de; heise@gfz-potsdam.de; sgming@gfz-potsdam.de; wickert@gfz-potsdam.de; zusflo@gfz-potsdam.de)